P Vacancy-Induced Electron Redistribution and Phase Reconstruction of CoFeP for Overall Water Splitting at Industrial Current Density

Xueling Wei[#], Yang Jiao[#], Xiangyu Zou*, Yuchen GUO[a], Wenhu Li*, Taotao Ai*

School of Material Science and Engineering, Shaanxi University of Technology, Hanzhong 723000, China

Supplementary information

List of contents

1. Experimental Section

1.1 Materials

Cobaltous nitrate hexahydrate ($Co(NO_3)_2·6H_2O$, 99.9%), Ferrous sulfate heptahydrate $FeSO_4·7H_2O$, 99.9%, Sodium hypophosphite NaH_2PO_2, potassium hydroxide (KOH), commercial ruthenium dioxide (RuO_2), and Nafion (5 wt%) were purchased from Shanghai Aladdin Biochemical Technology Co., Ltd. The deionized (DI) water used in the solution preparation and washing steps comes from ultrapure water (Milli-Q, 18 MΩ·cm) made in the laboratory. Nickel foam (NF, diameter of the nickel fiber: 1.6 mm, porosity: 96%) were used as the substrate. All chemicals were analytical grade and used as received without further purification.

1.2 Treatment of nickel foam

In order to remove the surface oxide layer, a piece of NF (1×3 cm^2) was treated in HCl solution (2.0 M) under ultrasonication for 0.5 h, followed by sonicating several times with ethanol and DI water successively, and finally dried in an oven at 60 °C for 6 h.

1.3. General characterizations

The microstructure and phase information of catalysts using X-ray diffraction (XRD, Rigaku Ultima IV, Cu Kα, λ = 1.54056 Å), field-emission scanning electron microscope (FESEM, JSM-7610F, 15 kV), and Transmission electron microscopy (TEM, JEOL 2010F) with EDS. The surface characteristics were investigated using X-ray photoelectron spectroscopy (XPS, Thermo Fisher Scientific K-Alpha, Mg Kα. In-situ Raman spectroscopy measurements were conducted using a confocal micro-Raman spectrometer (Renishaw inVia) coupled with an electrochemical workstation. The contents were determined using plasma optical emission spectrometry (ICP-OES, Agilent ICPOES730). The contact angle data of liquid and bubbles were recorded using a JY-82B instrument. The vacancies were characterized using EPR (BRUKER EMXPLUS).

1.4. Electrochemical test

Electrochemical measurements were conducted using a PARSTAT (P4000) workstation with a three-electrode configuration: Hg/HgO as the reference, graphite as the counter, and prepared samples as the working electrode.

The potentials were converted to the reversible hydrogen electrode (RHE) by the equation: $E_{RHE} = E_{Hg/HgO} + 0.098 + 0.0591 \times pH$. The catalytic performances of samples were evaluated using LSV at 5 mV s^{-1}.

All the LSV curves were derived from multiple tests to ensure data consistency. Electrochemical impedance spectroscopy (EIS) was conducted across a frequency from 10^5 to 10^{-2} Hz with 5 mV AC amplitude. The LSV curves were calibrated using a 70% solution resistance correction.

The electrochemically active surface area (ECSA) is directly proportional to the double-layer capacitance (C_{dl}) using the equation $ECSA = C_{dl} / C_s$, where C_s = 40 μF cm^{-2}. C_{dl} was determined from cyclic voltammograms at various scan rates in the non-Faradic potential region.The specific activity is the current density per unit real surface area of catalyst, which can be calculated by normalizing the current to the ECSA. The ECSA-normalized current density for the as-prepared catalysts was calculated according to: $j_{ECSA\text{-}normalized}=j/ECSA$

The Tafel slope was calculated according to Equation: $\eta = \alpha + \frac{2.3RT}{\alpha nF} log|j|$, where η is the overpotential, j is the current density, α is the transfer coefficient, n is the number of electrons involved in the reaction, F is the Faradaic constant, b = 2.3RTαnF is the value of Tafel slope.

Turnover frequency (TOF) calculation. TOF (for a heterogeneous catalyst) =j/(4*F*m). j: the current density at an overpotential; F: the Faraday constant; m: the number of moles of metal on the electrode.

The Faradaic efficiency for OER was tested at room temperature in a H-type cell. The oxygen evolution electrolysis was performed at a constant current of 0.3 A m^{-2} and oxygen was collected and measured. Faradaic efficiency (η) was calculated by Equation: $\eta = \frac{\eta_{experimental}}{\eta_{theoretical}} \times 100\%$. The theoretical number of moles ($\eta_{experimental}$) of oxygen produced was calculated by Equation: $\eta_{theoretical} = \frac{i \times t}{4 \times e \times N_A}$, where i (A) is the current, t (s) is the electrolysis time, e is the elementary charge (1.60×10^{-19} C), and N_A is the Avogadro's constant (6.02×10^{23}).

1.5. DFT calculation details

All the calculations were performed within the framework of density functional theory (DFT) using the projector augmented plane-wave method, as implemented in the Vienna ab initio simulation package (VASP). The generalized gradient approximation proposed by Perdew-Burke-Ernzerhof was selected for the calculation of exchange-correlation potentials. The cutoff energy for plane waves was set to 400 eV. The energy criterion was set to be 10^{-5} eV for obtaining the iterative solution of the Kohn-Sham equation. A 3 × 3 × 1 k-mesh was used for the structural optimizations of CoFeOOH, CoFeOOH-PO_4^{3-}, CoFeP, and $CoFeP_V$.

A 15 Å vacuum region was set in the z-direction to prevent interactions between two adjacent surfaces. The force and convergence thresholds for energy were less than

0.02 eV $Å^{-1}$ and 10^{-5} eV, respectively. During the calculations, the bottom layers of the structures were fixed. The reaction Gibbs free energy (ΔG) of the intermediates was determined using ΔG = ΔE + ΔZPE − TΔS, where T is the temperature (298.15 K), ΔZPE is zero-point energy, ΔE is the reaction energy, and ΔS is the entropy difference calculated from the vibration frequency. The entropies of H_2 and H_2O vapor under standard conditions were obtained from the NIST database.

2. Supplementary figures

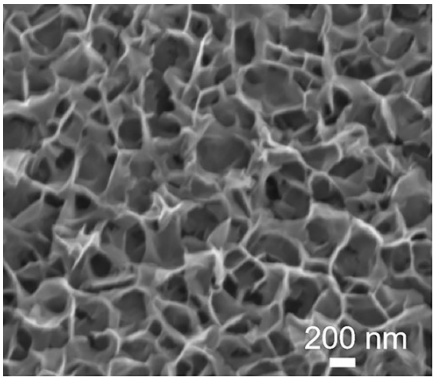

Fig S1. SEM image of CoFe@NF

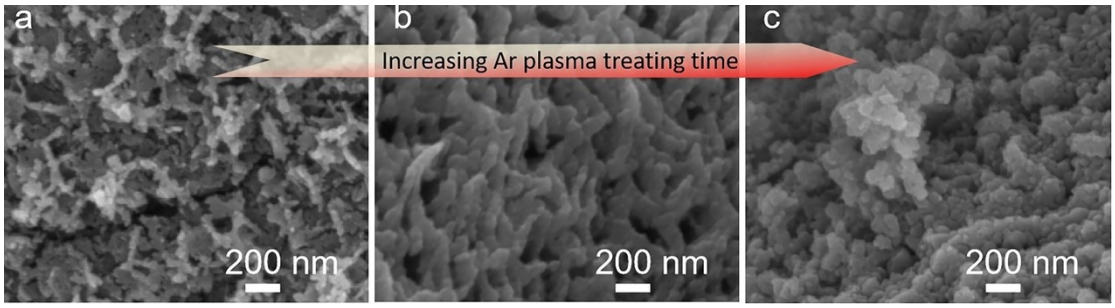

Fig S2. SEM images of CoFePv@NF with different plasma-assisted phosphating time (a) 3 min, (b) 6 min, (c) 9 min,

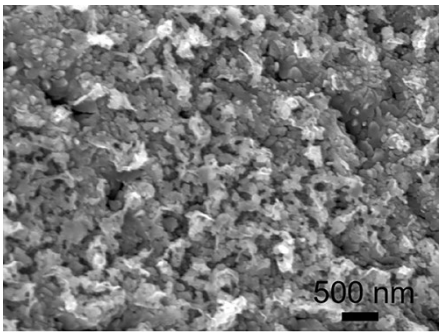

Fig S3. SEM image of CoFeP@NF

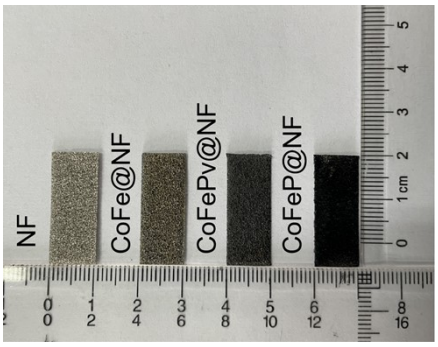

Fig S4. Photos of prepared electrodes

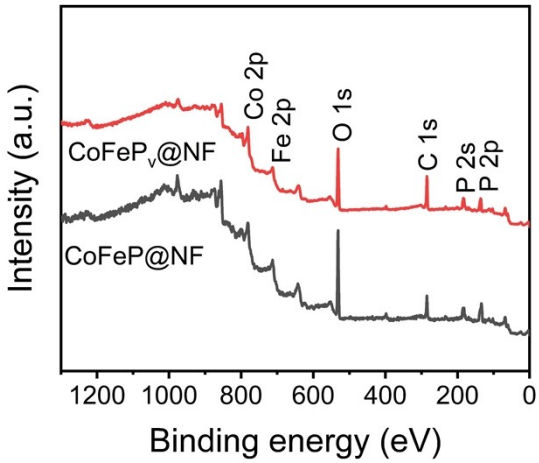

Fig S5. Full XPS spectrum of CoFeP$_v$@NF and CoFeP@NF

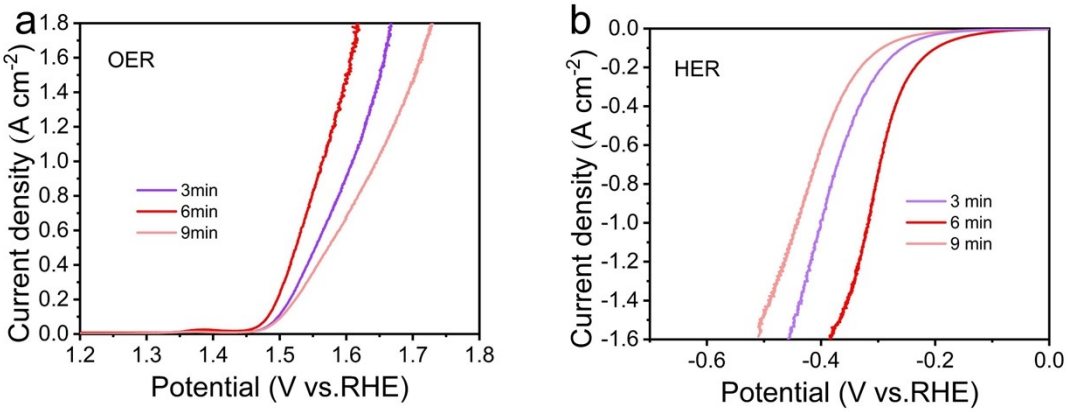

Fig. S6. Catalytic performance of CoFePv@NF with different plasma-assisted phosphating time (a) HER, (b) OER performance

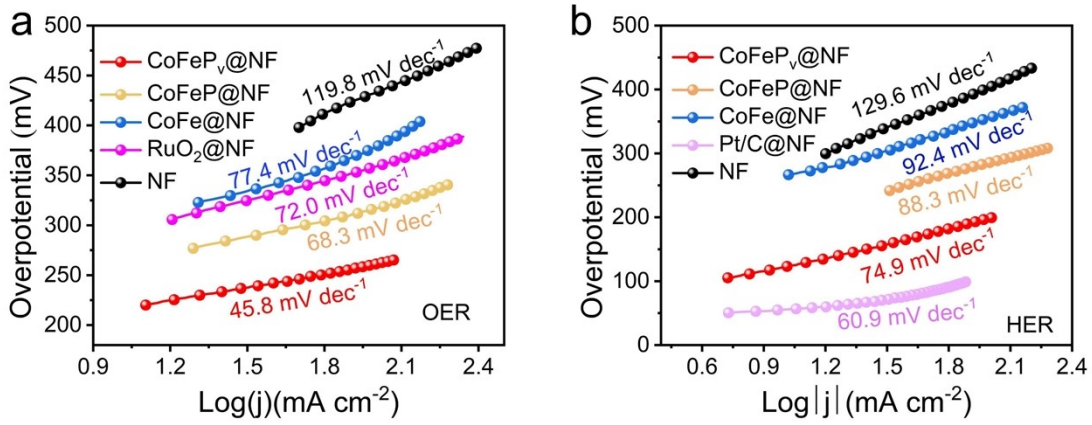

Fig S7. Tafel slopes of electrodes (a) OER, (b) HER

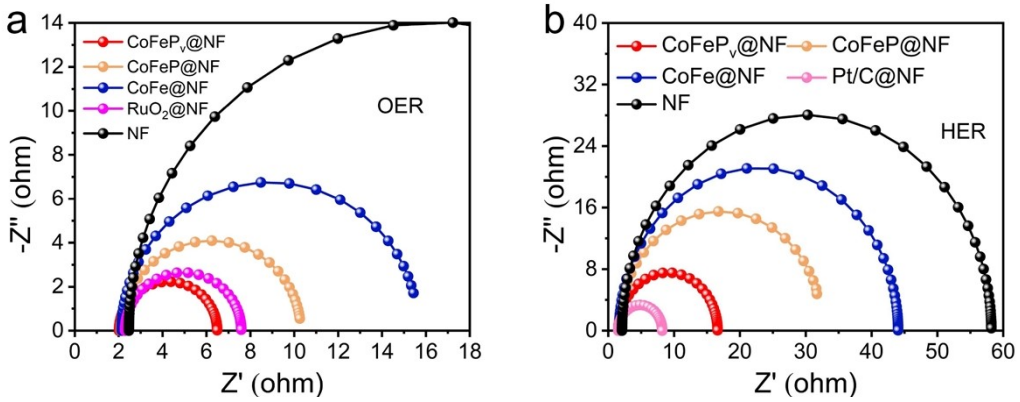

Fig S8. Nyquist plots of electrodes (a) OER, (b) HER

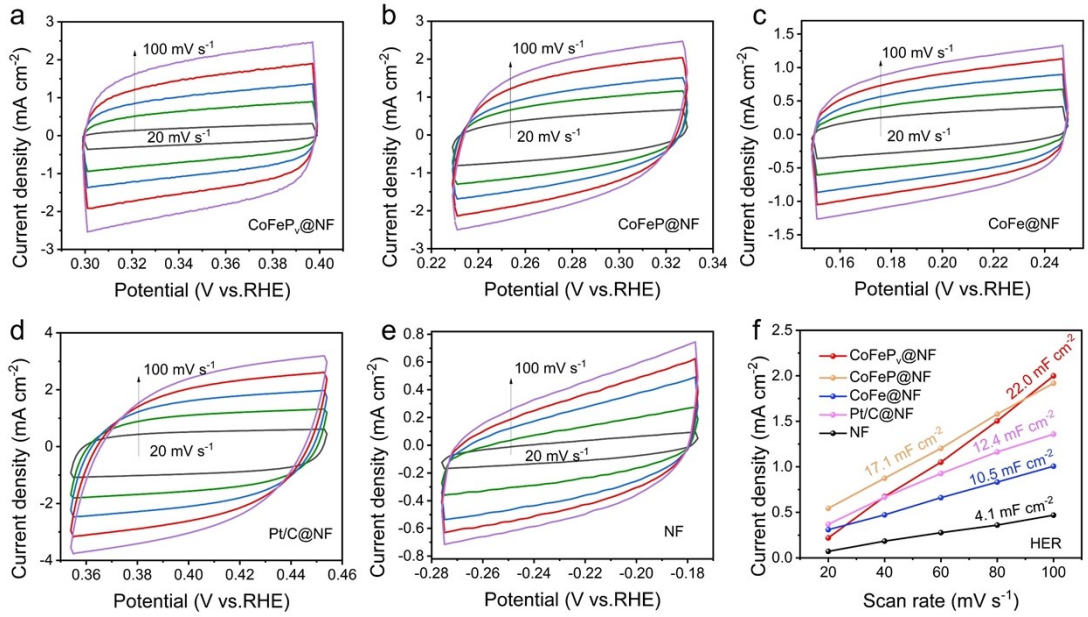

Fig S9. CVs in non-Farradic region at different scan rate for HER: (a) CoFePv@NF, (b) CoFeP@NF, (c) CoFe@NF, (d) Pt/C@NF, (e) NF, and (f) Corresponding C_{dl} by calculated

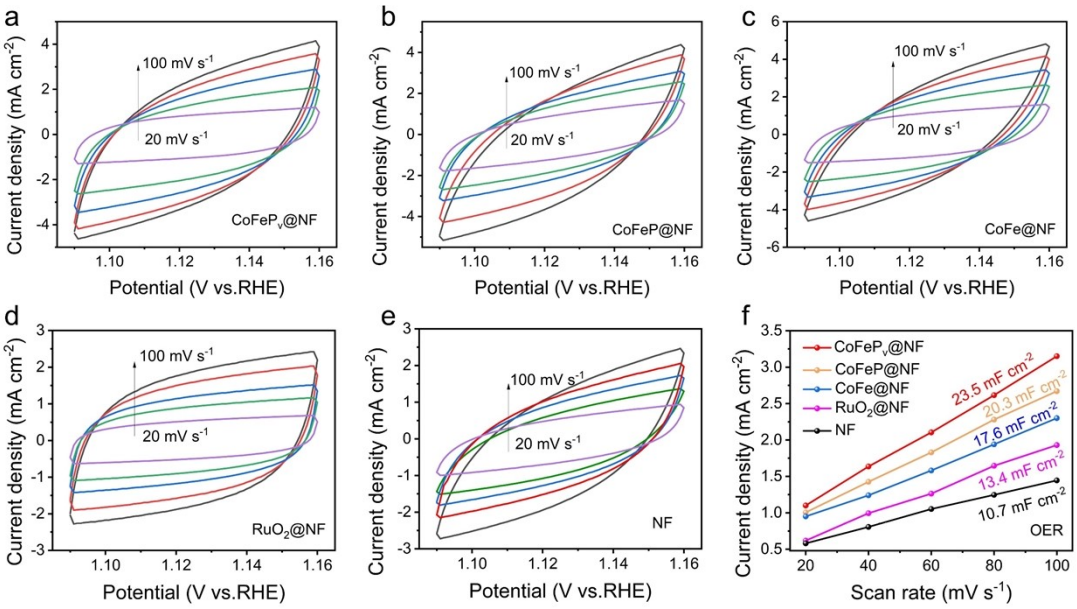

Fig S10. CVs in non-Farradic region at different scan rate for OER (a) CoFePv@NF, (b) CoFeP@NF, (c) CoFe@NF, (d) RuO_2@NF, (e) NF, and (f) Corresponding C_{dl} by calculated

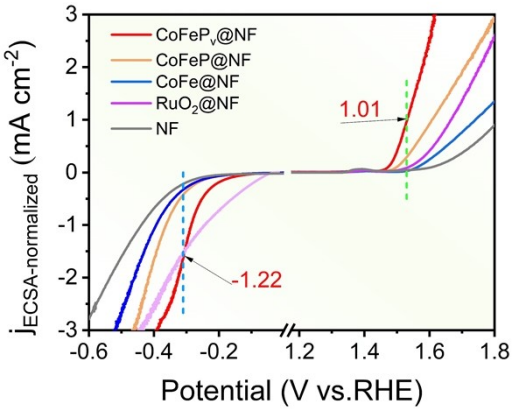

Fig S11. ECSA-normalized polarization curves

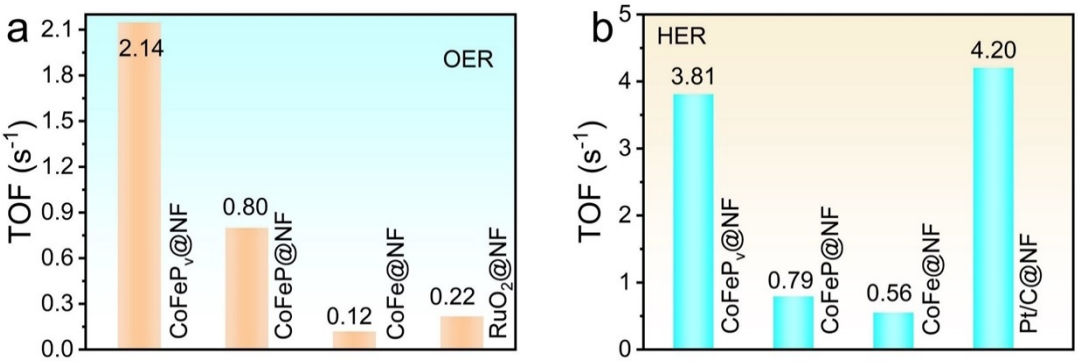

Fig S12. TOF of electrodes at the overpotential of 300 mV: (a) OER, (b) HER

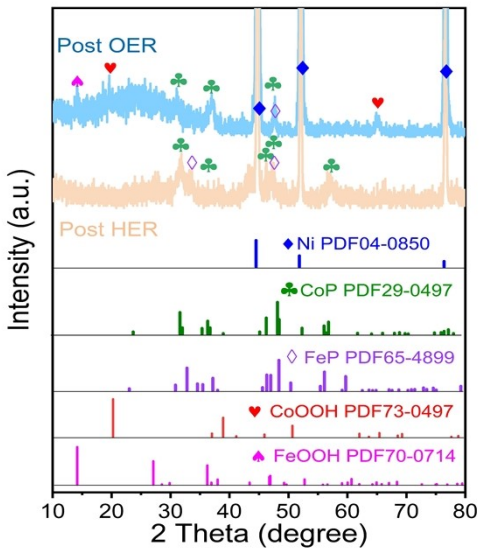

Fig S13.XRD patterns of CoFePv@NF after HER and OER stability test

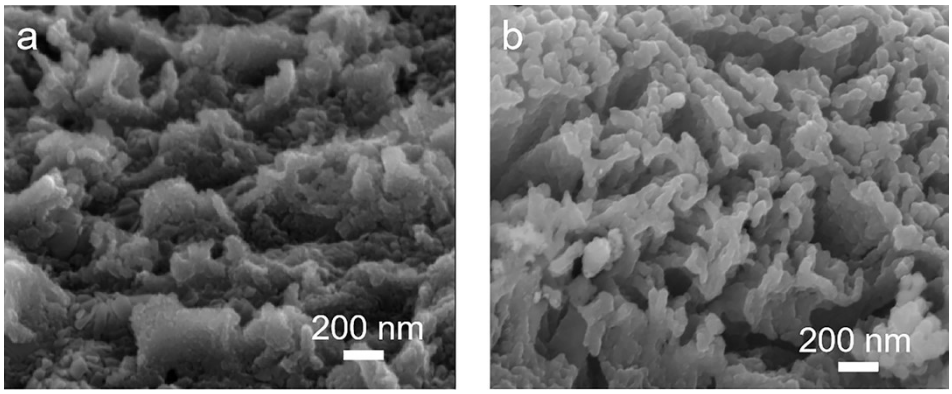

Fig S14. SEM images of CoFePv@NF after stability test: (a) HER, (b) OER

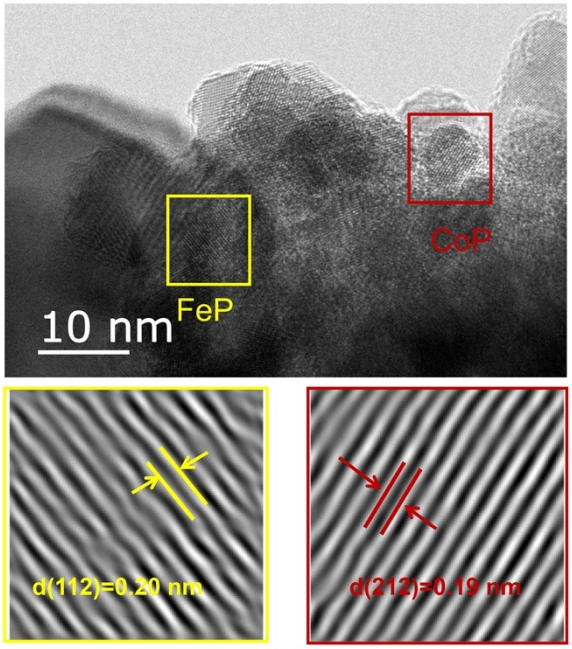

Fig S15. TEM images of CoFePv@NF after HER stability test

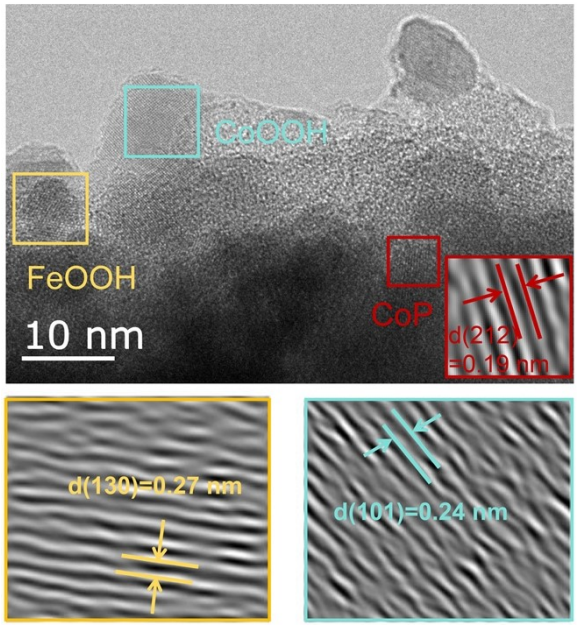

Fig. S16. TEM images of CoFePv@NF after OER stability test

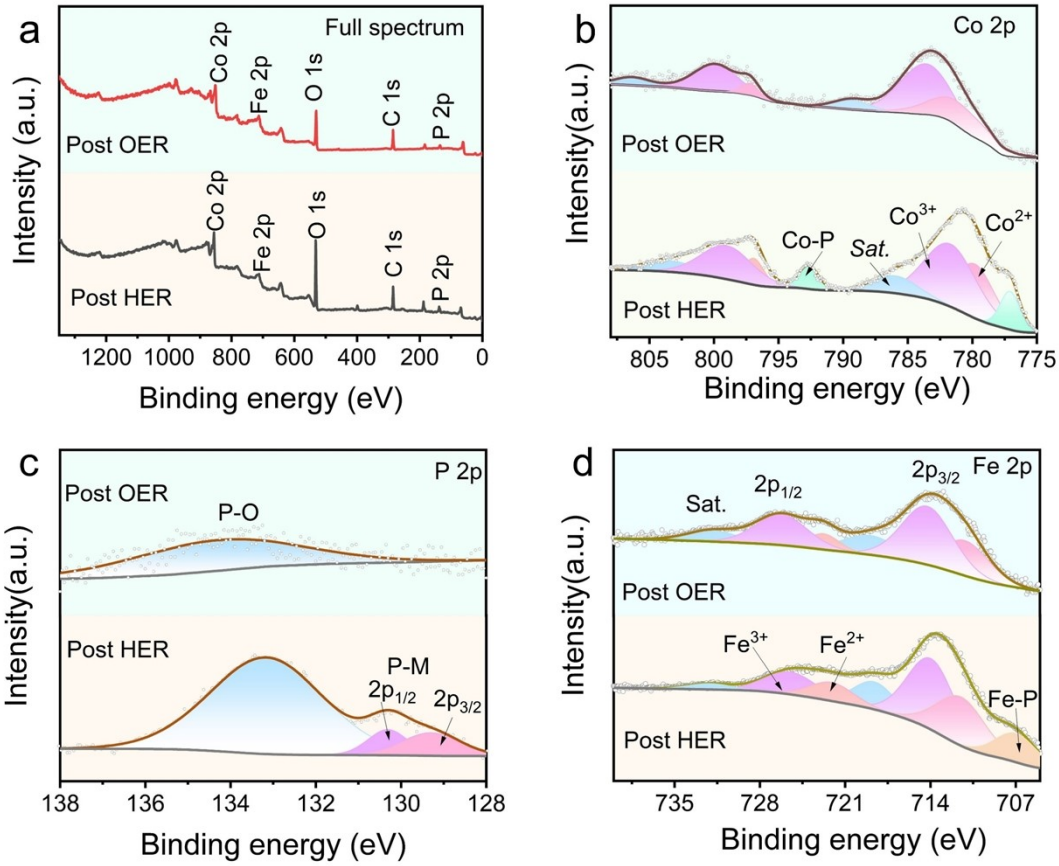

Fig. S17. XPS spectra of CoFePv@NF after HER and OER stability test:(a) Full spectrum, (b) Co 2p, (c) P 2p, (d) Fe 2p

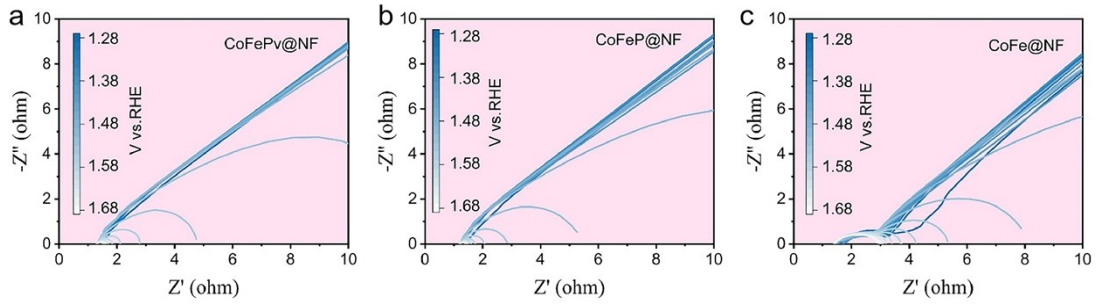

Fig. S18. In situ Nyquist plots of electrodes during OER (a) CoFePv@NF, (b) CoFeP@NF, (c) CoFe@NF

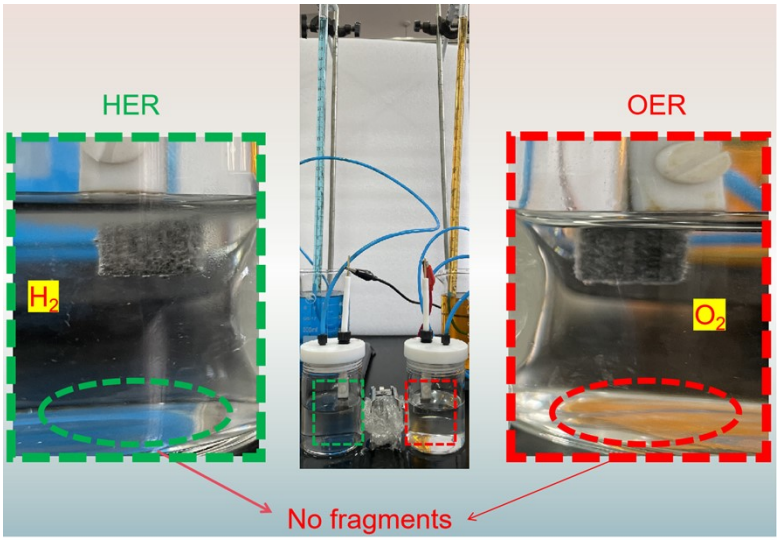

Fig.S19. The photo of drainage method

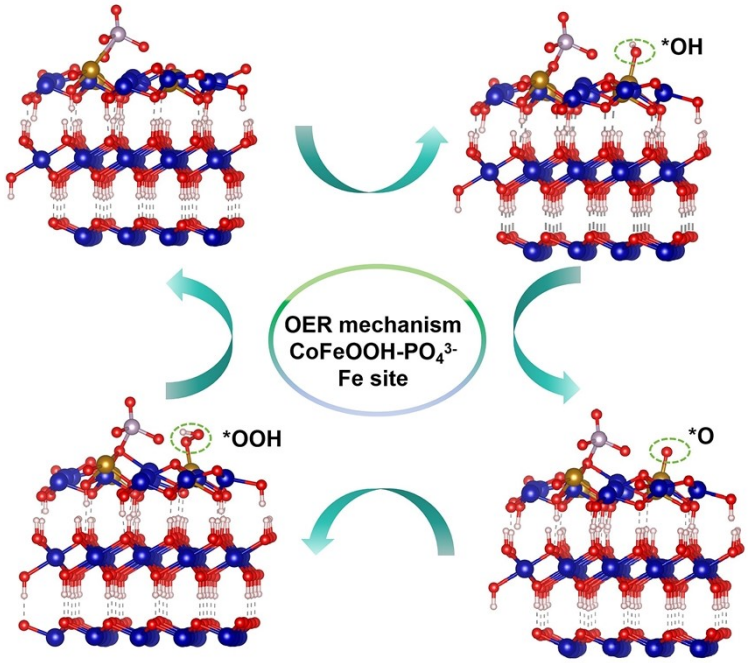

Fig. S20. OER mechanism of CoFeOOH-PO_4^{3-} at Fe sites

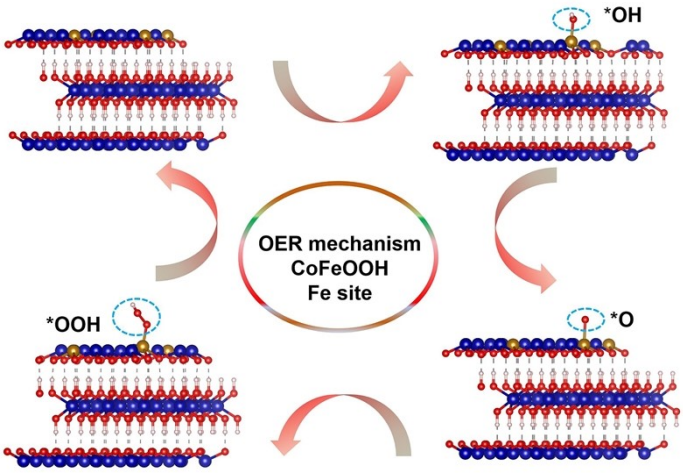

Fig. S21. OER mechanism of CoFeOOH at Fe sites

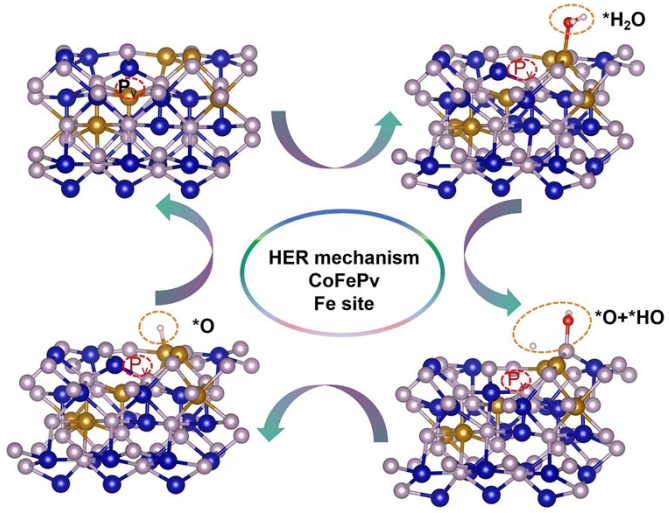

Fig. S22. HER mechanism of CoFePv at Fe sites

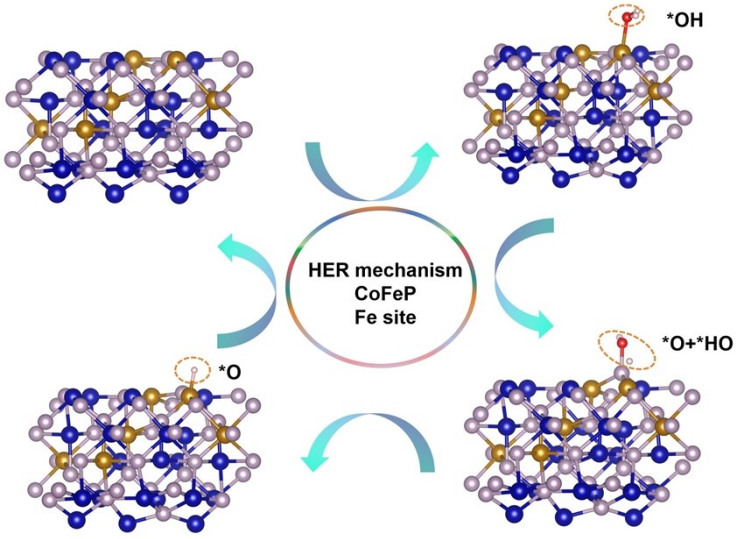

Fig. S23. HER mechanism of CoFeP at Fe sites

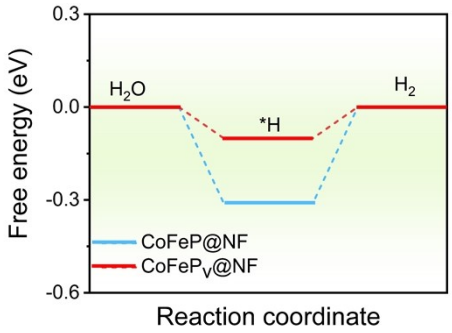

Fig. S24. HER pathway of CoFePv and CoFeP under alkaline conditions

Table S1 Mass ratios of CoFeP and CoFePv characterized by ICP-OES

Sample	Element	Mass-ratio (%)	Elements	Mass-ratio (%)	Elements	Mass-ratio (%)	Sum (%)
CoFeP	Co	72.23	Fe	26.64	P	1.13	100
CoFePv	Co	72.82	Fe	26.43	P	0.74	100

Table S2 Compared with other recent reported phosphate HER electrodes

Electrocatalysts	η_{10} (mV)	Tafel slope (mV dec^{-1})	References
CoFePv@NF	99	74.9	This work
CoPO@C/NF	93	111.4	[1]
CoP/$CoMoP_2$	93.6	89.9	[2]
1T′/1T Co,P-SnS_2@CC	94	75.2	[3]
Fe_2P-Co_2P-Ni_2P	105	86.09	[4]
NiSe2/Fe-P	113	73.1	[5]
CoP@PNC@NF	148	59.6	[6]
H-Fe_3O_4@FeP@NC	165	155.6	[7]
P-MoO_2@CoNiP	174	95.2	[8]
CoO/CoP-NC	178	90	[9]
Ni_2P-Fe_2P/NF	225	107	[10]
FeNiP-CoP@NC	254	24.9	[11]
Ni-FeP-B-0.02	337	74	[12]

Table S3 Compared with other recent reported phosphate OER electrodes

Electrocatalysts	η_{10} (mV)	Tafel slope (mV dec^{-1})	References
CoFePv@NF	243	45.8	This work
Co_2P-Co_xO_y	246	69	[13]
CoP-FeP/NC	254	50.9	[14]
H-Fe_3O_4@FeP@NC	258	41.3	[7]
Cu-Co-P/NF	259	57.99	[15]
FeCoP/C	282	53	[16]
Mn_1-Ni_1-Co_1-P/NF	289	85	[17]
Ni-CoP	290	66	[18]
Rh-Co_2Fe-P	303	63	[19]
CoNiFeP@NF	333	69	[20]
Co_2P/CoP@NPGC-1	340	116	[21]
CoP/CoP_2@NC	369	99	[22]
Fe-CoxP	440	49	[23]

Table S4 Compared with other recent reported phosphates OWS electrodes

electrodes	Voltage (V)	Ref.
CoFePv@NF(+, -)	1.9	This work
NiMoB||NiMoB(+, -)	2.11	[24]
FeIr/NF||FeIr/NF(+, -)	1.93	[25]
FeCoNiCu-PE(+, -)	1.931	[26]
FeCo/Ni$(OH_2$||Ni mesh(+, -)	1.91	[27]
$CoMoO_4$-$Co(OH)_2$/NF(+)||CoMoP-CoP/NF(−)	2.0	[28]
(Ni_3Fe−FeV_2O_4)@C/NF(+, -)	1.9	[29]

Fe-NiFe LDH(+, -)	2.0	[30]
Ru-Ni_2P/NiO/NF(+, -)	2.02	[31]
(NiCoRu)OH/S(+, -)	1.92	[32]
(NiFe)C_2O_4/NF||PtC	2.1	[33]
NiCo@C-NiCoMoO(+, -)	1.9	[34]
Co_4N-CeO_2(+, -)	1.97	[35]
Ru-CoO_x/NF(+, -)	1.92	[36]
NiFe/Ni/Ni(+, -)	1.96	[37]
Ni_3FeN/NF (+, -)	1.91	[38]

Reference

[1] S.-S. Xu, X.-W. Lv, Y.-M. Zhao, T.-Z. Ren, Z.-Y. Yuan, Engineering morphologies of cobalt oxide/phosphate-carbon nanohybrids for high-efficiency electrochemical water oxidation and reduction, J. Energy Chem., 52 (2021) 139-146, https://doi.org/10.1016/j.jechem.2020.04.054.

[2] L. Zhang, X. Shi, A. Xu, W. Zhong, J. Zhang, S. Shen, Novel CoP/$CoMoP_2$ heterojunction with nanoporous structure as an efficient electrocatalyst for hydrogen evolution, Nano Res., 17 (2024) 3693-3699, https://doi.org/10.1007/s12274-023-6270-1.

[3] M. Singh, T.T. Nguyen, M.A. P, Q.P. Ngo, D.H. Kim, N.H. Kim, J.H. Lee, Metallic metastable hybrid 1T/1T phase triggered Co,$PSnS_2$ nanosheets for high efficiency trifunctional electrocatalyst, Small, 19 (2023) 2206726, https://doi.org/10.1002/smll.202206726.

[4] T. Wang, F. Chen, J. Wang, C. Wang, L. Kuai, B. Geng, MOF-derived multicomponent Fe_2P-Co_2P-Ni_2P hollow architectures for efficient hydrogen evolution, Chem. Commun., 59 (2023) 298-301, https://doi.org/10.1039/D2CC06278J.

[5] J. Lin, H. Wang, Y. Yan, J. Cao, C. Qu, X. Zheng, J. Feng, J. Qi, Sandwich-like structured $NiSe_2$/Ni_2P@FeP interface nanosheets with rich defects for efficient electrocatalytic water splitting, J. Power Sources, 445 (2020) 227294,

https://doi.org/10.1016/j.jpowsour.2019.227294.

[6] N. Li, S. Qu, F. Qin, H. Li, W. Shen, Construction of P,N-codoped carbon shell coated CoP nanoneedle array with enhanced OER performance for overall water splitting, Int. J. Hydrogen Energy, 48 (2023) 27215-27230, https://doi.org/10.1016/j.ijhydene.2023.03.426.

[7] K. Chen, G.-C. Kim, C. Kim, S. Yadav, I.-H. Lee, Engineering core-shell hollow-sphere Fe_3O_4@FeP@nitrogen-doped-carbon as an advanced bi-functional electrocatalyst for highly-efficient water splitting, J. Colloid Interface Sci., 657 (2024) 684-694, https://doi.org/10.1016/j.jcis.2023.11.184.

[8] X. Yang, H. Bu, R. Qi, L. Ye, M. Song, Z. Chen, F. Ma, C. Wang, L. Zong, H. Gao, T. Zhan, Boosting urea-assisted water splitting over P-MoO_2@CoNiP through Mo leaching/reabsorption coupling CoNiP reconstruction, J. Colloid Interface Sci., 676 (2024) 445-458, https://doi.org/10.1016/j.jcis.2024.07.142.

[9] K. Chen, Y. Cao, W. Wang, J. Diao, J. Park, V. Dao, G.-C. Kim, Y. Qu, I.-H. Lee, Effectively enhanced activity for overall water splitting through interfacially strong P-Co-O tetrahedral coupling interaction on CoO/CoP heterostructure hollow-nanoneedles, J. Mater. Chem. A, 11 (2023) 3136-3147, https://doi.org/10.1039/D2TA08870C.

[10] Q. Zhang, X. Zeng, Z. Zhang, C. Jin, Y. Cui, Y. Gao, Electronic transfer and structural reconstruction in porous NF/FeNiP-CoP@NC heterostructure for robust overall water splitting in alkaline electrolytes, J. Colloid Interface Sci., 675 (2024) 357-368, https://doi.org/10.1016/j.jcis.2024.07.019.

[11] L. Wu, L. Yu, F. Zhang, B. McElhenny, D. Luo, A. Karim, S. Chen, Z. Ren, Heterogeneous bimetallic phosphide Ni_2P-Fe_2P as an efficient bifunctional catalyst for water/seawater splitting, Adv. Funct. Mater., 31 (2021) 2006484, https://doi.org/10.1002/adfm.202006484.

[12] J. Hu, J. Yin, A. Peng, D. Zeng, J. Ke, J. Liu, K. Guo, In situ hydroxide growth over nickel-iron phosphide with enhanced overall water splitting performances, Small, 20 (2024) 2402881, https://doi.org/10.1002/smll.202402881.

[13] G. Huang, M. Hu, X. Xu, A.A. Alothman, M.S.S. Mushab, S. Ma, P.K. Shen, J.

Zhu, Y. Yamauchi, Optimizing heterointerface of Co_2P-CoO nanoparticles within a porous carbon network for deciphering superior water splitting, Small Struct., 4 (2023) 2200235, https://doi.org/10.1002/sstr.202200235.

[14] Z. Li, X. Wang, Y. Xu, X. Li, J. Zhang, Y. Liu, J. Luo, Y. Zhou, Hollow nanocubic CoP-FeP/NC heterostructures for efficient electrocatalytic oxygen evolution reaction, Fuel, 371 (2024) 131838, https://doi.org/10.1016/j.fuel.2024.131838.

[15] R. Deng, Q. Zhang, Cu embedded in Co-P nanosheets with super wetting structure for accelerated overall water splitting under simulated industrial conditions, Adv. Energy Mater., 14 (2024) 2401444, https://doi.org/10.1002/aenm.202401444.

[16] R. Zhao, B. Ni, L. Wu, P. Sun, T. Chen, Carbon-based iron-cobalt phosphate FeCoP/C as an effective ORR/OER/HER trifunctional electrocatalyst, Colloids Surf., A, 635 (2022) 128118, https://doi.org/10.1016/j.colsurfa.2021.128118.

[17] K.E. Salem, A.A. Saleh, G.E. Khedr, B.S. Shaheen, N.K. Allam, Unveiling the optimal interfacial synergy of plasma-modulated trimetallic Mn-Ni-Co phosphides: tailoring deposition ratio for complementary water splitting, Energy Environ. Mater., 6 (2023) e12324, https://doi.org/10.1002/eem2.12324.

[18] Y. Zhao, J. Zhang, Y. Xie, B. Sun, J. Jiang, W.-J. Jiang, S. Xi, H.Y. Yang, K. Yan, S. Wang, X. Guo, P. Li, Z. Han, X. Lu, H. Liu, G. Wang, Constructing Atomic Heterometallic Sites in Ultrathin Nickel-Incorporated Cobalt Phosphide Nanosheets via a Boron-Assisted Strategy for Highly Efficient Water Splitting, Nano Lett., 21 (2021) 823-832, https://doi.org/10.1021/acs.nanolett.0c04569.

[19] L. Li, Y. Lu, X. Liu, X. Wang, S. Zhou, Layered double hydroxide drived ultra-evenly Rh-doped Co_2Fe-P composite for high-efficient overall water splitting, J. Alloys Compd., 895 (2022) 162549, https://doi.org/10.1016/j.jallcom.2021.162549.

[20] Y. Kuang, S. Zhao, S. Gao, N. Song, CoNi-phosphides with iron incorporation effectively boost hydrogen evolution reaction and oxygen evolution reaction for overall water splitting, Int. J. Hydrogen Energy, 83 (2024) 1184-1192, https://doi.org/10.1016/j.ijhydene.2024.08.208.

[21] W. Gong, H. Zhang, L. Yang, Y. Yang, J. Wang, H. Liang, Core@shell MOFs derived Co_2P/CoP@NPGC as a highly-active bifunctional electrocatalyst for

ORR/OER, Ind. Eng. Chem., 106 (2022) 492-502, https://doi.org/10.1016/j.jiec.2021.11.032.

[22] X. Liu, J. Wu, Z. Luo, P. Liu, Y. Tian, X. Wang, H. Li, Co_2P-assisted atomic Co-N_4 active sites with a tailored electronic structure enabling efficient ORR/OER for rechargeable Zn–Air batteries, ACS Appl. Mater. Interfaces, 15 (2023) 9240-9249, https://doi.org/10.1021/acsami.2c19713.

[23] W. Song, X. Teng, Y. Niu, S. Gong, X. He, Z. Chen, Self-templating construction of hollow Fe-Co_xP nanospheres for oxygen evolution reaction, Chem. Eng. J., 409 (2021) 128227, https://doi.org/10.1016/j.cej.2020.128227.

[24] R. Mandavkar, M.A. Habib, S. Lin, R. Kulkarni, S. Burse, J.-H. Jeong, J. Lee, Electron enriched ternary NiMoB electrocatalyst for improved overall water splitting: Better performance as compared to the Pt/C||RuO_2 at high current density, Applied Materials Today, 29 (2022) 101579, https://doi.org/10.1016/j.apmt.2022.101579.

[25] J. Chen, Y. Wang, G. Qian, T. Yu, Z. Wang, L. Luo, F. Shen, S. Yin, In situ growth of volcano-like FeIr alloy on nickel foam as efficient bifunctional catalyst for overall water splitting at high current density, Chem. Eng. J., 421 (2021) 129892, https://doi.org/10.1016/j.cej.2021.129892.

[26] R. Feng, Z. Ye, Q. Jiang, C. Li, J. Gu, F. Song, Phosphorus-doping promotes the electrochemical etching of metals to nanoporous electrodes for efficient and durable overall water splitting, J. Power Sources, 542 (2022) 231774, https://doi.org/10.1016/j.jpowsour.2022.231774.

[27] S. Xu, C. Chen, J. Shen, Z. Xu, Y. Lu, P. Song, W. Dong, R. Fan, M. Shen, The bifunctional 3D-on-2D FeCo/$Ni(OH)_2$ hierarchical nanocatalyst for industrial-level electrocatalytic water splitting, Int. J. Hydrogen Energy, 48 (2023) 17882-17893, https://doi.org/10.1016/j.ijhydene.2023.01.289.

[28] P. Yan, Y. Qin, Y. Yang, X. Shao, T.T. Isimjan, X. Yang, Controllable transformation of sheet-like CoMo-hydro(oxide) and phosphide arrays on nickel foam as efficient catalysts for alkali water splitting and Zn-H_2O cell, Int. J. Hydrogen Energy, 47 (2022) 23530-23539, https://doi.org/10.1016/j.ijhydene.2022.05.136.

[29] H. Wang, X. Chen, H. Yu, X. Liang, Z. Li, M. Hu, L. Yang, P. Tsiakaras, S. Yin,

In-situ adsorption and catalysis of polysulfide on Janus Ni_3Fe-Fe_2VO_4 heterostructure for Li -S batteries, Chem. Eng. J., 487 (2024) 150669, https://doi.org/10.1016/j.cej.2024.150669.

[30] M. Mehdi, B.-S. An, H. Kim, S. Lee, C. Lee, M. Seo, M.W. Noh, W.-C. Cho, C.-H. Kim, C.H. Choi, B.-H. Kim, M. Kim, H.-S. Cho, Rational design of a stable Fe-rich Ni-Fe layered double hydroxide for the industrially relevant dynamic operation of alkaline water electrolyzers, Adv. Energy Mater., 13 (2023) 2370108, https://doi.org/10.1002/aenm.202370108.

[31] H. Zhang, X. Wu, C. Chen, C. Lv, H. Liu, Y. Lv, J. Guo, J. Li, D. Jia, F. Tong, Spontaneous ruthenium doping in hierarchical flower-like Ni_2P/NiO heterostructure nanosheets for superb alkaline hydrogen evolution, Chem. Eng. J., 417 (2021) 128069, https://doi.org/10.1016/j.cej.2020.128069.

[32] Y. Yang, R. Chen, J. Dai, D. Guo, L. Liu, Scale-up synthesis of RuCoNi hydroxide/sulfide heterostructures in alkali for the industrial current density, Chem. Eng. J., 474 (2023) 145971, https://doi.org/10.1016/j.cej.2023.145971.

[33] Z. Li, Y. Yao, S. Sun, J. Liang, S. Hong, H. Zhang, C. Yang, X. Zhang, Z. Cai, J. Li, Y. Ren, Y. Luo, D. Zheng, X. He, Q. Liu, Y. Wang, F. Gong, X. Sun, B. Tang, Carbon oxyanion self-transformation on NiFe oxalates enables long-term ampere-level current density seawater oxidation, Angew. Chem. Int. Ed., 63 (2024) e202316522, https://doi.org/10.1002/anie.202316522.

[34] G. Qian, J. Chen, T. Yu, L. Luo, S. Yin, N-doped graphene-decorated NiCo alloy coupled with mesoporous NiCoMoO nano-sheet heterojunction for enhanced water electrolysis activity at high current density, Nano-Micro Lett., 13 (2021) 77, https://doi.org/10.1007/s40820-021-00607-5.

[35] H. Sun, C. Tian, G. Fan, J. Qi, Z. Liu, Z. Yan, F. Cheng, J. Chen, C.-P. Li, M. Du, Hybrid nanosheet arrays: boosting activity on Co_4N porous nanosheet by coupling CeO_2 for efficient electrochemical overall water splitting at high current densities Adv. Funct. Mater., 30 (2020) 2070213, https://doi.org/10.1002/adfm.202070213.

[36] D. Wu, D. Chen, J. Zhu, S. Mu, Ultralow Ru incorporated amorphous cobalt-based oxides for high-current-density overall water splitting in alkaline and seawater media,

Small, 17 (2021) 2102777, https://doi.org/10.1002/smll.202102777.
[37] P.-c. Wang, L. Wan, Y.-q. Lin, B.-g. Wang, NiFe hydroxide supported on hierarchically porous nickel mesh as a high-performance bifunctional electrocatalyst for water splitting at large current density, ChemSusChem, 12 (2019) 4038-4045, https://doi.org/10.1002/cssc.201901439.
[38] H. Hu, X. Wang, Z. Zhang, J. Liu, X. Yan, X. Wang, J. Wang, J.P. Attfield, M. Yang, Engineered nickel-iron nitride electrocatalyst for industrial-scale seawater hydrogen production, Adv. Mater., n/a (2024) 2415421, https://doi.org/10.1002/adma.202415421.